CFD Simulation of Multiphase Flow at Different Scales

Minsheng Zhao, Xiaosong Zhang, Xiao Wen, Jianhua Wang, Cheng Liu, Decheng Wan*
Collaborative Innovation Center for Advanced Ship and Deep-Sea Exploration, State Key Laboratory of Ocean Engineering, School of Naval Architecture, Ocean and Civil Engineering, Shanghai Jiao Tong University
Shanghai, China
* Corresponding Author: dcwan@sjtu.edu.cn

ABSTRACT

Along with advances in computer technology, numerical simulation has been widely used in the analysis of marine hydrodynamic problems, especially for the multiphase flow. According to the resolution-scales, the simulation of multiphase flow can be performed in macroscale, mesoscale and microscale, corresponding numerical methods, i.e. the RANS/DES approach with VOF method, Euler-Lagrange method, Moving Particle Semi-implicit (MPS) method and DNS method, are demonstrated in the present paper. The numerical results obtained by those methods are in consistent with the experimental ones and other's research. It is concluded that with further development of theoretical study and numerical methods, the present numerical methods can deal with complex multiphase flow problems in multiple scales. Efficiency and accuracy need to be focused in the future development of the numerical model and CFD solver.

KEY WORDS: Multiphase flow; cavitation; breaking wave; bubble flow; MPS method

INTRODUCTION

Multiphase flows are complex phenomena and can be found in a variety of situations, both in natural and industrial process. The complexity of multiphase flow increases with the presence of multiscale turbulence, large-density-ratio two-phase flow and complicated boundaries. Although the research of multiphase flow is challenging, related studies are of great importance in theoretical analysis and practical applications for the development of many interfacial-flow-equipment.

In the field of ship and ocean engineering, there are many topics related to multiphase flow and its branches. The wave-making of surface ships, wave-structure interaction, breaking waves, bubble flow and cavitation, are typical features of multiphase flow in ship and ocean engineering. The in-depth study of gas-liquid two-phase flow lays a foundation for numerical simulation of various multiphase flows. The multiphase flow can be classified into three categories according to the resolved flow feature scales, i.e. macroscale, mesoscale and microscale multiphase flows. The macroscale multiphase flow is mainly computed through relatively simplified models, where the interface is not actually tracked. The Volume of Fluid (VOF) method is one of the approaches for macroscale multiphase flow. The mesoscale flow is generally resolved by the Euler-Lagrange method, while the microscale multiphase flow is that all the interface features are computed directly. The meshless method, such as MPS and SPH method, can give the detailed description of the microscale features since the interface is actually tracked. The DNS approach can also be one of the approaches to predict the microscale multiphase flow behavior. Over the past decade, the Computational Marine Hydrodynamics Lab (CMHL) in Shanghai Jiao Tong University has focused on the development of numerical schemes and solvers related to multiphase flow. So far, the self-developed CFD solvers have been successfully applied to the numerical study on different scales of multi-phase flows, such as ship hydrodynamics, cavitation flow, offshore platform in waves, wave-breaking and floating offshore wind turbines. The recent progress on numerical simulation of multiphase flow at different scales by CMHL are demonstrated in the present paper, where the cavitation flow and ship breaking bow waves at macroscale, bubble flow at mesoscale and various multiphase flows at microscale are illustrated in detail.

MACROSCALE FLOW

Breaking Wave

Breaking wave is one of the most complex free surface flows in ship and ocean engineering and it is also very difficult to resolve the interface. So far, we have conducted numerical predictions of breaking waves based on RANS/DES approach incorporating with VOF method to capture free surface. In general, the two-phase flow in ship and ocean engineering is treated as incompressible and immiscible flow. The governing equations for the two-phase flow follows:

$$\nabla \cdot \mathbf{U} = 0 \tag{1}$$

$$\frac{\partial \rho \mathbf{U}}{\partial t} + \nabla \cdot (\rho(\mathbf{U} - \mathbf{U}_g)\mathbf{U}) = -\nabla p_d - \mathbf{g} \cdot \mathbf{x} \nabla \rho + \nabla \cdot (\mu_{eff} \nabla \mathbf{U}) + \nabla \mathbf{U} \cdot \nabla \mu_{eff} + \boldsymbol{f}_\sigma \tag{2}$$

where p_d is the dynamic pressure of flow field obtained by subtracting the hydrostatic part $\rho \mathbf{g} \cdot \mathbf{x}$ from total pressure; $\mathbf{g}$ is gravitational acceleration vector; $\mu_{eff} = \rho \nu_{eff}$ denotes the effective dynamic viscosity of fluid; $\boldsymbol{f}_\sigma = \sigma \kappa \nabla \alpha$ is the source term for surface tension, with σ the surface tension coefficient, κ the mean curvature of the interface and α denotes the volume fraction. In OpenFOAM, VOF method with bounded compression technique[1] is applied to capture free surface and the transport equation is expressed as:

$$\frac{\partial \alpha}{\partial t} + \nabla \cdot \left[\left(\mathbf{U} - \mathbf{U}_g \right) \alpha \right] + \nabla \cdot \left[\mathbf{U}_r \left(1 - \alpha \right) \alpha \right] = 0 \tag{3}$$

where α is volume of fraction, 0 and 1 represent that the cell is filled with air and water respectively and $0 < \alpha < 1$ stands for the interface between two-phase fluid. $\boldsymbol{U}_r$ in Eqn.错误!未找到引用源。 is the velocity field used to compress the interface and it only takes effect on the free surface due to the term $(1-\alpha)\alpha$.

Currently, the in-house solver naoe-FOAM-SJTU [2-4] supports $k-\omega$ SST and $k-\omega$ SST DES/DDES model. Both URANS and DES/DDES computations can be performed when simulating the two-phase flows. The eddy viscosity in these models are calculated by:

$$\nu_t = \frac{a_1 k}{\max(a_1 \omega, F_2 \Omega)} \tag{4}$$

in which k and ω are turbulence kinetic energy (TKE) and specific turbulence dissipation rate, respectively; a_1 is model coefficient; F_2 is the blending function; Ω is the vorticity.

For URANS, the k and ω are solved by the following transport equations:

$$\frac{\partial (\rho k)}{\partial t} + \nabla \cdot (\rho k \mathbf{U}) = \rho \tilde{G} - \rho \frac{k^{3/2}}{l_{RANS}} + \nabla \cdot \left[\rho \left(\nu + \alpha_k \nu_t \right) \nabla k \right] \tag{5}$$

$$\frac{\partial (\rho \omega)}{\partial t} + \nabla \cdot (\rho \omega \mathbf{U}) = \rho \gamma S^2 - \rho \beta \omega^2 + \nabla \cdot \left[\rho \left(\nu + \alpha_\omega \nu_t \right) \nabla \omega \right] + \rho (1 - F_1) C D_{k\omega} \tag{6}$$

where, $l_{RANS} = \sqrt{k} / (\beta^* \omega)$ is the RANS turbulent length scale.

The $k-\omega$ SST DES/DDES modifies the length scale to become l_{DES} and l_{DDES}, respectively, defined as:

$$l_{DES} = \min(C_{DES} \Delta, l_{RANS}) \tag{7}$$

$$l_{DDES} = l_{RANS} - f_d \max(0, l_{RANS} - C_{DES} \Delta) \tag{8}$$

in which, C_{DES} is the calibrated DES constant; Δ is the grid scale; f_d is a delayed function which ensures that DES works in RANS manner inside boundary layer to avoid Grid-Induced Separation (GIS).

Based on the above numerical models and schemes, the present solver has been applied to simulate breaking bow waves for high-speed ships. VOF method with bounded compression technique is utilized to capture the free surface. Wang et al.[5] firstly conducted the predictions of breaking bow waves for DTMB 5415 at two approaching speeds corresponding to Froude number of Fr=0.35 and Fr=0.41. During the simulations, the model was held fixed with sinkage and trim set to the values previously determined in unrestrained conditions[6]. Two grids are adopted in the simulation of Fr=0.35 case, one has 18.7 million cells and another one has 12 million cells with no refinement in the bow region. Fig. 1 shows the comparison of the wave patterns with different grids. The finer mesh can give promising result of the bow wave pattern according to the experimental measurements, where two scars can be formed due to the plunger breaker of the ship bow waves. In addition, the present approach can also give good prediction of the wake flow around ship hull. The detailed comparison of the wake flow in different sections with the available experimental measurements can be found in the Wang et al.[5]

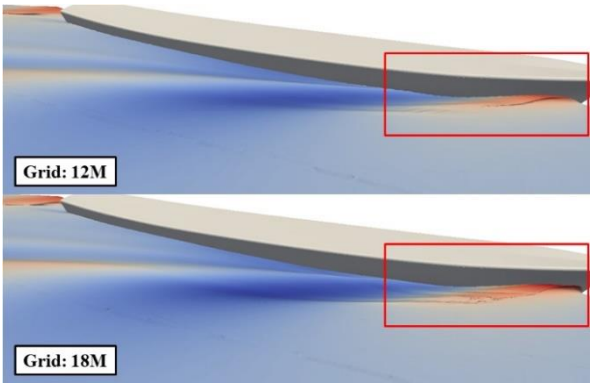

Figure 1 Wave pattern with different grids

Despite the simulations of the break bow waves of DTMB 5415 ship model, the break wave of KCS ship has also been investigated using different turbulence models. Both RANS can DDES computations were conducted by Wang et al.[7] to find a suitable model to give better description of break bow wave phenomenon. Grid density study was firstly performed to evaluate how much grid was needed to resolve the breaking waves and it was concluded that a grid size around $\Delta x / L = 1 \times 10^{-3}$ in three directions was required to capture the breaking bow waves.

The numerical results of RANS and DDES approach were also validated by the available experiments. The breaking wave phenomena can be observed from all three approaches, while the experimental measurement shows more violent behavior toward the back of the wave. Higher speed, Fr=0.40 experiences rough breaking bow waves and seems more unsteady. Figure. 2 presents the comparison of all three approaches.

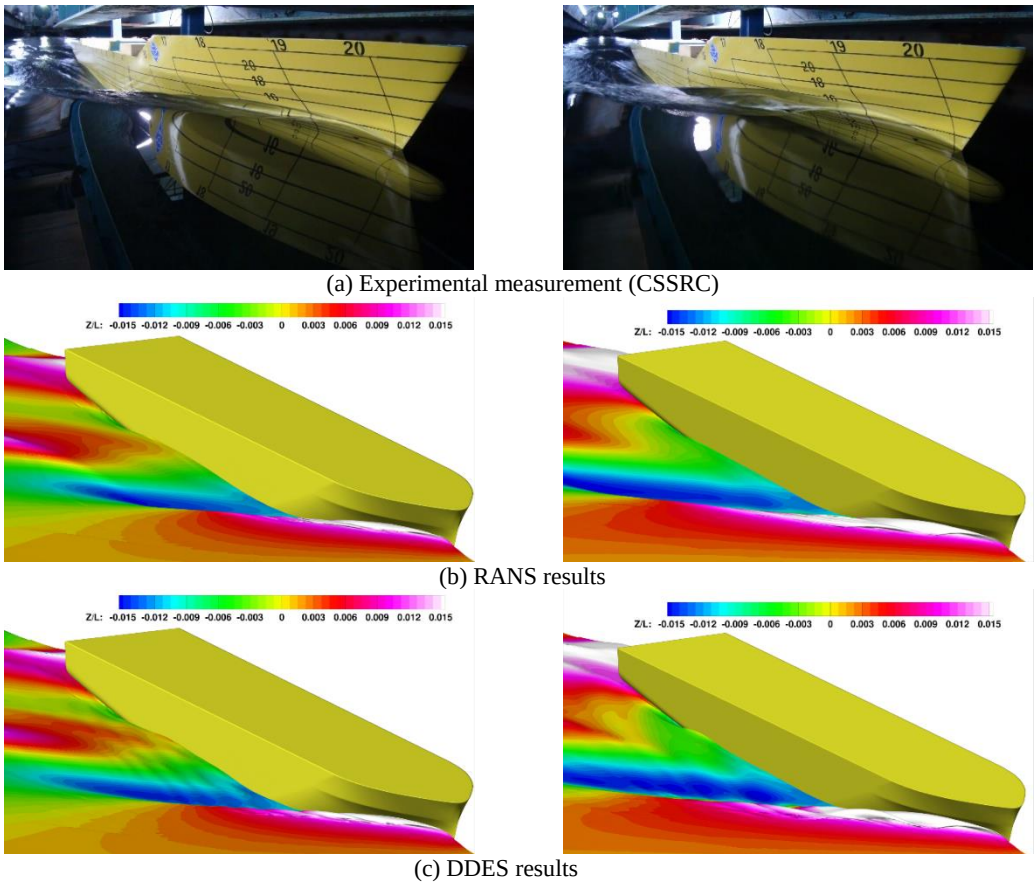

(a) Experimental measurement (CSSRC)

(b) RANS results

(c) DDES results

Figure 2 Comparison of wave pattern (left column: Fr=0.35, right column: Fr=0.40)

The evolution of bow waves along the longitudinal direction showed two plungers with obvious air entrainment, which is consistent with the measurements. The wave-making phenomenon was more violent in the DDES results, which shows good agreement with the experiment. Detailed flow information, such as wave profiles at hull surface, vorticity field around free surface, was also presented to illustrate the flow characters. It was shown that the variation

of vorticity is mainly concentrated near the free surface. The vorticity dissipated quickly in the present RANS computation, leading to the significant difference of the bow waves compared with the DDES results. Though there is no available experimental flow data to validate the present computation results, it is still convincible that the DDES approach is more appropriate for the simulation of high speed ships, especially when considering the breaking waves.

Cavitation Flow

Cavitation is a complex flow phenomenon including unsteady characteristics, turbulence, gas-liquid two-phase flow. Due to the unsteady characteristics of the cavitation bubble, the pressure fluctuation during the collapse stage of the cavitation bubble will cause noise and vibration. Cavitation flow belongs to two-phase flow and there is continuous mass transformation between vapor phase and liquid phase in the two-phase flow. In order to solve a cavitation flow problem, despite the continuity equation and momentum equations, the phase equation should also be solved. In the present paper, the mass transfer model which also called cavitation model is applied to solve the cavitation flow. The cavitation model adopted here was developed by Schnerr and Sauer[8]. In their papers, the vapor fraction is related to the number of gas nucleus per unit volume and the average radius of gas nucleus. The condensation and evaporation rates are defined as follows:

$$\alpha_v = n_0 \frac{4}{3}\pi R^3 / (n_0 \frac{4}{3}\pi R^3 + 1) \tag{9}$$

$$\dot{m}_c = C_c \frac{3\rho_v \rho_l \alpha_v (1-\alpha_v)}{\rho R} \mathrm{sgn}(P_v - P) \sqrt{\frac{2|P_v - P|}{3\rho_l}} \tag{10}$$

$$\dot{m}_v = C_v \frac{3\rho_v \rho_l \alpha_v (1-\alpha_v)}{\rho R} \mathrm{sgn}(P_v - P) \sqrt{\frac{2|P_v - P|}{3\rho_l}} \tag{11}$$

R is the average radius of gas nucleus expressed as

$$R=(\frac{\alpha_v}{1-\alpha_v} \cdot \frac{3}{4\pi n_0})^{1/3} \tag{12}$$

The parameter n_0 is the number of gas nucleus per unit volume as an important parameter for the description of mass transfer rates between vapor and fluid. It needs to be provided as input. In this paper, it is set with a default value of 1.6e+13.

Turbulence model plays an important role in the numerical simulation of cavitation flows. The SST k-omega turbulence model which developed by Menter is mixed with the k-omega model in the near-wall area and the k-epsilon model in the far field. Reboud[9] gave the suggestion that an artificial reduction of the turbulent viscosity of this model can predict a more accurate frequency of the periodical shedding of cavitation. So, a serial of modified SST k-omega models is applied following his idea:

$$\mu_t = f(\rho) C_\omega \frac{k}{\omega} \tag{13}$$

$$f(\rho) = \rho_v + \frac{(\rho_m - \rho_v)^n}{(\rho_l - \rho_v)^{n-1}}; n \gg 1 \tag{14}$$

Figure 3 Distribution of interface of the simulation and the experiment

The abscissa represents the dimensionless parameter x/D, while the ordinate represents pressure coefficient. The point whose value in the abscissa is 0 represents the apex of the cylinder. The solid line in red color is the simulation value, and the point in blue color is the experimental value. We can see that the pressure coefficient decreases sharply with the increase of the value in the abscissa. When the pressure coefficient reduces to -0.4, cavitation occurs rapidly. Then the pressure coefficient begins to recover when the value in the abscissa increases to approximately 1. We can consider that the section of the solid line where the value of pressure distribution

coefficient is -0.4 represents the region that cavitation occurs. The length of the region is about 0.6 D. The graph of pressure distribution coefficient gives us an indirect observation on the cavitation area, while the graph of alpha.water gives a direct approach. The distribution of alpha.water of the simulation and the experiment is shown in Fig. 3, as well as an isosurface of the vapor fraction in Fig. 4. As can be observed, the simulated results agrees well with the experimental data both in the distribution of pressure coefficient and alpha.water.

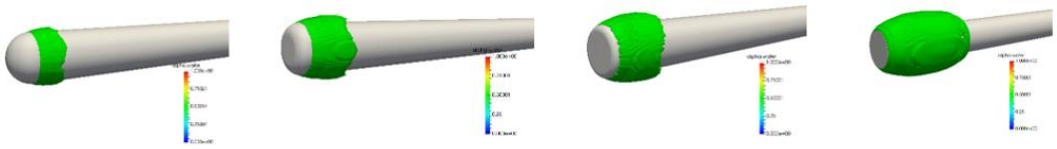

Figure 4 Cavitation area indicated by an isosurface of the vapor fraction (alpha.water = 0.5)

Then the pressure coefficient in different cavitation numbers is shown in Fig. 5. The simulation results show that the cavitation doesn't occur when the cavitation number is 0.6, which correspond to the conclusion of experiments that the critical cavitation number in this case is 0.6. Compared with the lines in cavitation number 0.4 and 0.2, it can be found that the lengths of cavitation area are in a great difference. The former one is 2.6 D while the latter is 0.6 D. It shows that the cavitation numbers have a great influence on the characteristic parameters of cavitation. The smaller the cavitation number, the longer the length of the cavitation. The differences between different head shapes also are shown in Fig.5. The red solid line, the blue solid line, the red dotted line and the green solid line in the right graph in Fig. 5 correspond to four cases that the chamfer radius vary from 0.5D to 0. It can be seen that as the radius of the lead angle decreases, the length of the cavitation increases. The reason for this phenomenon is that the smaller the radius of the chamfer angle, the smaller the collision buffer between the upstream flow and the cylinder top. So, the amplitude and the area of pressure reduction are really large, and the recovery of pressure becomes hard, which finally lead to the larger length of cavitation.

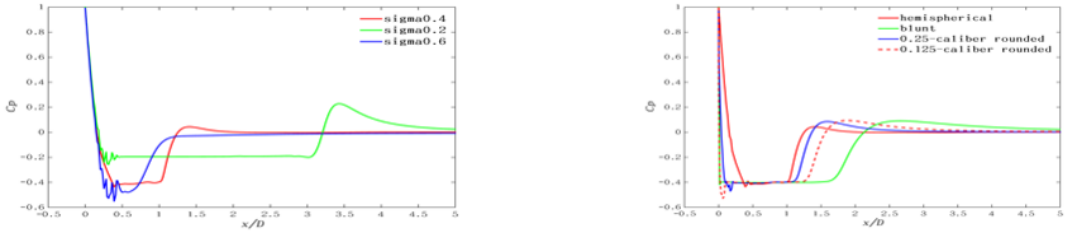

Figure 5 Pressure coefficient in different cavitation numbers(left) and pressure coefficient with different head shapes(right)

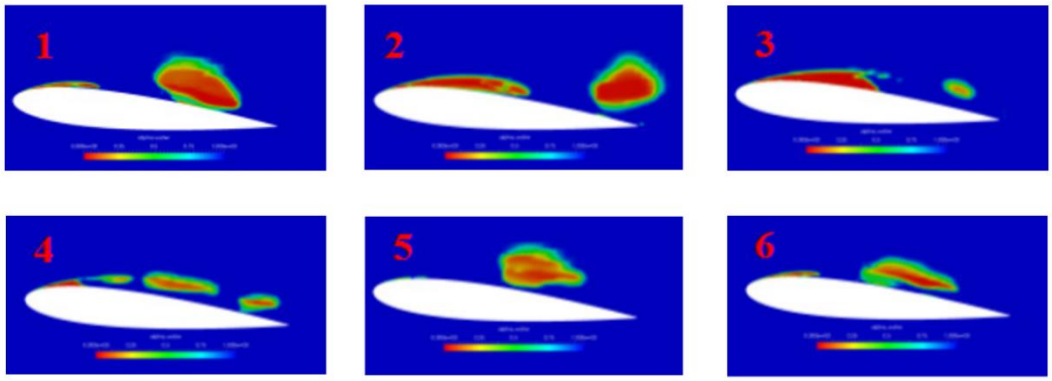

Figure 6 Periodical change in the shape of cavitation with modified SST k-omega model

The simulation of NACA0015 in cavitation with modified SST k-omega turbulence model obviously performs better in capturing small vortices structures during the whole period of cavitation development. In Fig. 4, the voids consisting of micro-voids and droplets with very small thickness are first generated at the head of the hydrofoil. At that time the cavity is still attached to the surface of the hydrofoil. With the passage of time, the attached cavities continue to develop towards the tail of the hydrofoil. The thickness of the cavity increases along the direction of the wing chord and gradually reaches its maximum, and the end of the cavity is at the tail of the hydrofoil. At the same time, small vortices fall off at the end of the cavity. Then, the cavity breaks into two parts, the front part is attached

to the suction surface of the hydrofoil, and the tail section of the cavity forms the shedding of large cavitation and moves downstream.

The retraction at the junction between the end of the inner cavity and the hydrofoil indicates that there is a re-entrant jet, which results in small bubbles falling off at the end of the inner cavity. In Fig. 6, the incoming flow flows into the middle of the hydrofoil, resulting in unstable cloud cavitation, which moves downward from the hydrofoil to form distinct cloud droplets. The calculated results basically describe the fracture and detachment behavior in the process of cavitation, which are in good agreement with the experimental results.

The velocity vector diagram during cavitation separation is shown in Fig. 7. Analyzing the velocity vector diagram, the re-entrant jet in the margin between the cavitation and wall, and the vortex which occurs in the tail region during the growth of sheet cavitation are accurately predicted. Vortex structure leads to the re-entrant jet, which leads to the cloud cavitation due to the sheering action during the collision. Hence the vortex is actually the cause for cavitation shedding.

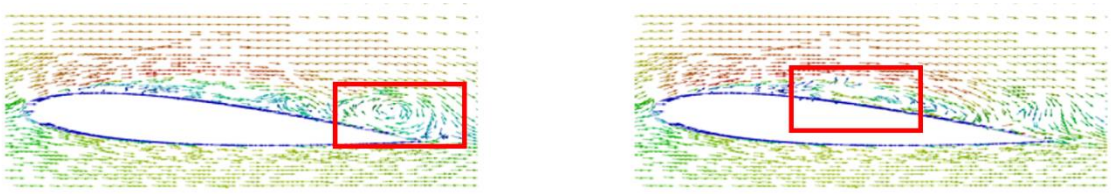

(a) Vortex structure (b) Re-entrant jets

Figure 7 Velocity vector of the flow fields at different time

MESOSCALE FLOW

The Euler-Lagrange Method in Mesoscale Simulation of Bubble Flow

In the solution of continuous-discrete phase systems with high void fractions, mesoscale method can present more details of mutiphase flow than macroscale method, and it requires less computational resources than the microscale method. The various behaviors of discrete particle phase including movement, collision, breakup and coalescence can be solved by using mesoscale method. But flows below the particle scale cannot be resolved. Interparticle forces arising from van der Waals, electrostatic, and liquid-bridge interactions are readily included[10]. There are several kinds of typical mesoscale method, such as Euler-Lagrange Method, Generalized Population Balance Equation Method[11] and Energy-minimization Multi-scale Method[12]. At present, our group mainly adopts The Euler-Lagrange Method in mesoscale simulation of bubble flow.

In Eulerian-Lagrangian method, continuous phase (liquid) and discrete phase (bubbles) are treated in different frameworks. The liquid flow is solved in the Euler framework, whose governing equations are the Navier-Stokes equations. While the bubbles are tracked by the kinematic equation following Newton's second law. The governing equations of liquid and bubbles are shown as follows:

$$\frac{\partial \overline{u_i}}{\partial x_i} = 0 \tag{15}$$

$$\frac{\partial \overline{u_i}}{\partial t} + \overline{u_j}\frac{\partial \overline{u_i}}{\partial x_j} = -\frac{1}{\rho}\frac{\partial \overline{p}}{\partial x_i} - \frac{\partial}{\partial x_j}\left(\overline{\sigma_{ij}} + \tau_{ij}\right) + \frac{f_{l-b}}{\rho} \tag{16}$$

$$m\frac{dv}{dt} = f_{l-b} + f_g + f_c = \frac{3mC_D}{4d}|u-v|(u-v) + \frac{m\rho_l}{\rho_b}C_L(u-v)\times(\nabla\times u) + C_V\left(\frac{Du}{Dt} - \frac{dv}{dt}\right) + mg\left(1-\frac{\rho_l}{\rho_b}\right) + \sum_{j=1}^{N} f_{c_j} \tag{17}$$

The coupling effect between liquid and bubbles is achieved by force f_{l-b}. The first three terms on the right side of the equation Eqn.(17) represent the forces acting on the bubble by the liquid, namely the drag force, lift force and the added mass force, respectively. Drag coefficient C_D, lift coefficient C_L and add mass coefficient C_V are determined by constitutive models. According to the Newton's third law, the hydrodynamic forces on all bubbles in each grid are added up and averaged by grid volume, and finally are added as source term to the liquid momentum equation Eqn.(16). This process is called two-way coupling. The fourth term of the equation Eqn.(17) is the gravity-buoyancy. The last term represents the bubble-bubble collision and bubble-wall collision. A non-linear spring-dashpot-slider model is used to calculate contact forces. On the basis, the coalescence and breakup

of bubbles can also be solved. This process is called four-way coupled. The open source CFD platform OpenFOAM is utilized in our work to develop a complete four-way coupled computational program. The default gas-solid solver has been optimized for bubble flow simulation by implanting models related to bubbles. In addition, the coalescence modules and breakup modules are also developed in our present solver. The solving process of the bubble flow Euler-Lagrange solver is shown in Fig. 8.

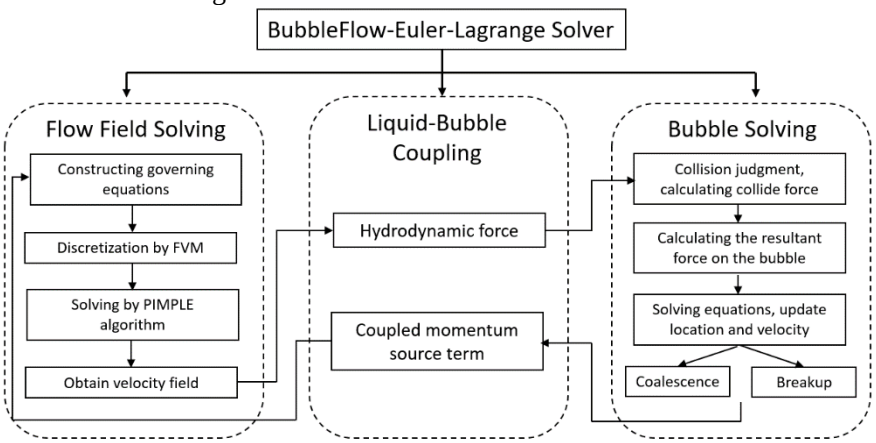

Figure 8 The solving process of the bubble flow Euler-Lagrange solver

The present bubble flow Euler-Lagrange solver has been applied to investigate the microbubble drag reduction. Microbubble drag reduction technology takes advantage of blower and porous plate to inject microbubbles to the bottom of ship, which can significantly reduce frictional resistance. Many experiments have confirmed the prominent drag reduction effect of microbubbles. However, the deep mechanism still needs to be further studied by numerical simulation. By using the solver introduced above, a turbulent channel flow laden with microbubbles is simulated firstly. The liquid phase is solved using LES method and the impact of microbubbles on the drag force, mean velocity profile, turbulent intensities and Reynolds stress are investigated.

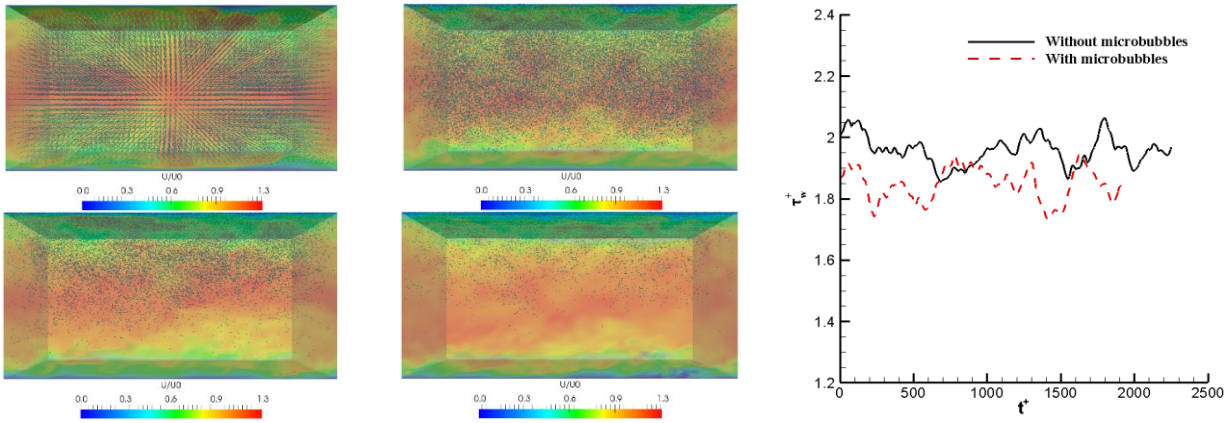

(a) (b)

Figure 9 Microbubble transport process in the channel and Time history of steady state frictional drag coefficient

As shown in Fig. 9 (a), the buoyancy force from the large density difference leads to the floating motion of bubbles to the upper wall gradually. Microbubbles attached to the wall can change the local viscosity, which contribute to the drag reduction. Fig. 9 (b) shows the drag reduction effect of the upper wall in the steady state. Quantitatively, about 6% drag reduction effect is obtained. The effect not only comes from the change of local viscosity, but also comes from the inhibition of turbulent vortexes.

In addition, the solver has also been applied to investigate the skin-friction drag reduction on a flat plate with bubble injection on the top and bottom of the plate. The simulated condition is the same as the experiment of Yan et al.[13]. The comparison of typical bubble flow field can be seen in Fig. 10. Under the action of buoyancy, the degree of adhesion between bubbles and the lower surface of the plate is greater than that of the upper surface. Thus, the lower surface has better drag reduction effect at low flow velocity and the upper surface has better drag reduction effect at high flow velocity. The bubble flow field in the experiment can be well reproduced by numerical simulation.

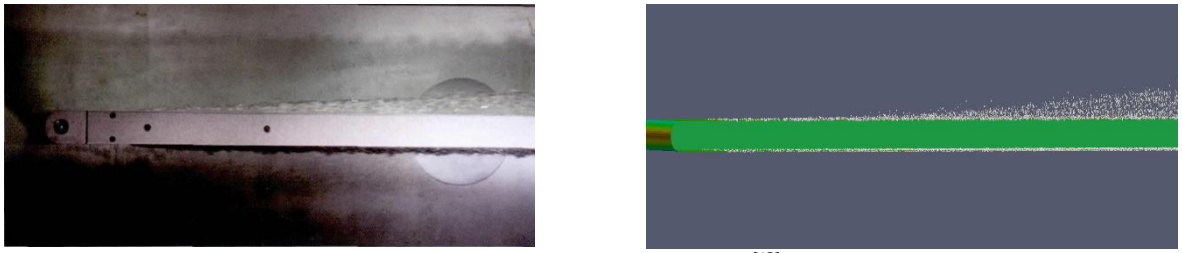

Figure 10 Typical bubble flow field of experimental results[13] and numerical results.

MICROSCALE FLOW

Moving Particle Semi-implicit Method

For Eulerian grid methods, sophisticated algorithms need to be included to capture the multiphase interface, such as the Level Set method (LS), Volume of Fluid method (VOF) and front tracking method. However, these algorithms complicate the computation process and greatly affect the numerical stability and accuracy. In recent few years, the Lagrangian particle methods develop rapidly and are considered as a better choice for multiphase flows. In particles methods, the particles with distinct physical properties are defined to represent the flow field. Following the governing equations, the particles can freely move and the multiphase interface is naturally obtained from the particle's distribution in calculation domain, thus making the approach can resolve the microscale interface flow.

In our CMHL group, an in-house single-phase solver MLParticle-SJTU has been firstly developed based on the Moving Particle Semi-implicit method (MPS). And then the MLParticle-SJTU is extended to multiphase flows by introducing a new MPS multiphase model. Successful applications of the new model have been made in some typical multiphase problems, including Rayleigh-Taylor instability 错误!未找到引用源。 and multi-layer-liquid sloshing 错误!未找到引用源。. The advantage of MPS multiphase model in capturing complicate interface also makes us believe its huge potential in the numerical study of cavitation, especially when we care about the details of cavitation bubble deformation. For this purpose, some preliminary work has been done and will also be presented later.

In present MPS multiphase method, the motion of particles is governed by the continuity and momentum equations based on Lagrangian description, expressed as follow:

$$\frac{D\rho}{Dt} = -\rho(\nabla \cdot \mathbf{u}) = 0\,,\ \rho\frac{D\mathbf{u}}{Dt} = -\nabla P + \nabla^2\mathbf{u} + \mathbf{g} + \mathbf{F}_s \tag{18}$$

where $\mathbf{F}_s$ is the interface tension force between different phases, which can be calculated with the surface tension coefficient and interface curvature. To replace all terms of differential operators in the right hand of governing equations, particle interaction models are used, including gradient model, divergence model and Laplacian model:

$$\left\langle \frac{1}{\rho}\nabla P \right\rangle_i = \frac{1}{\rho_i}\frac{d}{n^0}\sum_{j\neq i}\frac{\left(P_j - P_i\right)}{r_{ij}^{\,2}}\mathbf{e}_{ij}W\left(r_{ij}, r_e\right) \tag{19}$$

$$\left\langle \nabla \cdot \mathbf{u} \right\rangle_i = \frac{d}{n^0}\sum_{j\neq i}\frac{\left(\mathbf{u}_j - \mathbf{u}_i\right)}{r_{ij}^{\,2}} \cdot \mathbf{e}_{ij}W\left(r_{ij}, r_e\right) \tag{20}$$

$$\left\langle \nabla^2 P^{k+1} \right\rangle_i = \frac{2d}{n^0\lambda}\sum_{j\neq i}(P_j - P_i)\cdot W(r_{ij}, r_e) \tag{21}$$

where $W\left(r_{ij}, r_e\right)$ represents the strength of the interaction between two arbitrary particle *i* and *j*, and λ is a parameter introduced to keep the increase of variance equal to analytical solution.

In our solver, the two-phase system is treated as a unified system with multi-density and multi-viscosity field. The mathematical discontinuity of density and viscosity at interface, which causes a discontinuous acceleration field and accordingly numerical instabilities, brings the greatest challenge. Therefore, additional interface treatments are adopted.

To reduce the viscosity discontinuity, an inter-particle viscosity 错误!未找到引用源。 between particles of different phases is introduced, based on the harmonic mean of different viscosity. And the viscous term in momentum equation can be rewritten.

$$\mu\nabla^2 \cdot \mathbf{u} = \frac{2d}{n^0\lambda}\sum_{j\neq i}\mu_{ij}(\mathbf{u}_j - \mathbf{u}_i)W(r_{ij}, r_e)\,,\quad \mu_{ij} = \frac{2\mu_j\mu_i}{\mu_j + \mu_i} \tag{22}$$

To smooth density, a simple spatial averaging of density is conducted for interface particles [错误!未找到引用源。], which is effective for the multiphase problems with low density ratio.

$$\rho_i = \frac{\sum_{j\in i} \rho_j W\left(r_{ij}, r_e\right)}{\sum_{j\in i} W\left(r_{ij}, r_e\right)} \tag{23}$$

However, the density smoothing is less effective for the cases with high density ratio, due to the overestimation of pressure gradient force exerted on lighter particles by heavier particles. In our solver, an improved pressure gradient model with inter-particle density [错误!未找到引用源。] is employed to keep the continuity of acceleration induced by pressure gradient.

$$\left\langle \frac{1}{\rho}\nabla P \right\rangle_i = \frac{d}{n^0}\sum_{j\neq i} \frac{2\left(P_j - P_i\right)}{\rho_i + \rho_j} \cdot \frac{\mathbf{e}_{ij}}{r_{ij}^2} W\left(r_{ij}, r_e\right) + \frac{d}{n^0} \cdot \frac{\left(P_i - P_{i,\min}\right)}{\rho_i} \cdot \sum_{j\neq i} \frac{\mathbf{e}_{ij}}{r_{ij}^2} W\left(r_{ij}, r_e\right) \tag{24}$$

where the first term of right hand represents the original pressure gradient model but with a arithmetic mean inter-particle density, and the second term is a particle stabilizing term (PST) to exert a artificial force with a direction from a dense particle region to a dilute one.

In MPS method, the pressure field is obtained by solving a Pressure Poisson Equation (PPE). In present multiphase model, an improved PPE considers both the stability and air compressibility is employed [错误!未找到引用源。].

$$\left\langle \nabla^2 P^{k+1} \right\rangle_i = (1-\gamma)\frac{\rho}{\Delta t}\nabla \cdot \mathbf{u}_i^* - \gamma \frac{\rho}{\Delta t^2} \frac{\left\langle n^k \right\rangle_i - n^0}{n^0} + \frac{1}{\rho \Delta t^2 C_s^2} P_i^{n+1} \tag{25}$$

where the first and second term of right hand represent divergence-free and constant particle number density condition for incompressible flows, respectively. The last term is a compressible term calculated according to equation of state (EOS).

Numerical Examples

In this section, the new multiphase method is applied to simulate two-dimensional bubble rising and verified against quantitative benchmark in open literature [错误!未找到引用源。]. The initial condition is shown in Fig. 11(a), where a lighter bubble is surrounded by a heavier liquid in a rectangular tank. The density ratio is 1000/100 and the parameters keep consistent with the quantitative benchmark. In this case, the surface tension effects are strong enough compared with gravitational forces and can hold the bubble together during the rising process and the rising bubble ends up in the ellipsoidal regime, as shown in Fig. 11(b, c, d).

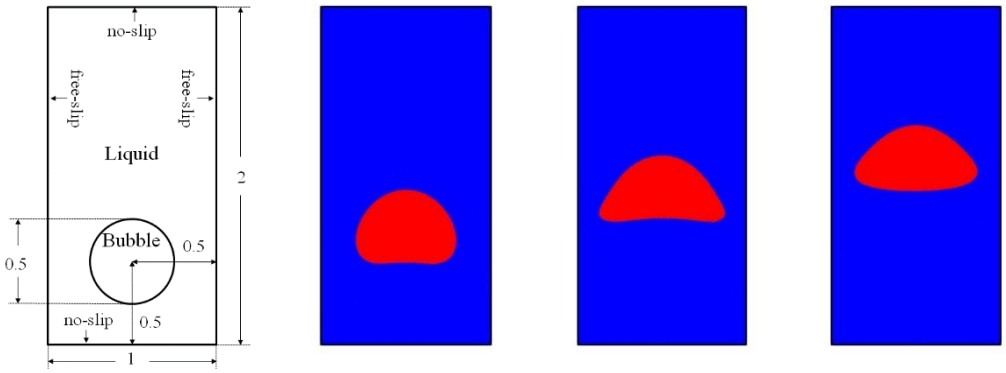

(a) Initial condition (b) t = 1 s (c) t = 2 s (d) t = 3 s

Figure 11 Time evolution of the rising bubble shapes

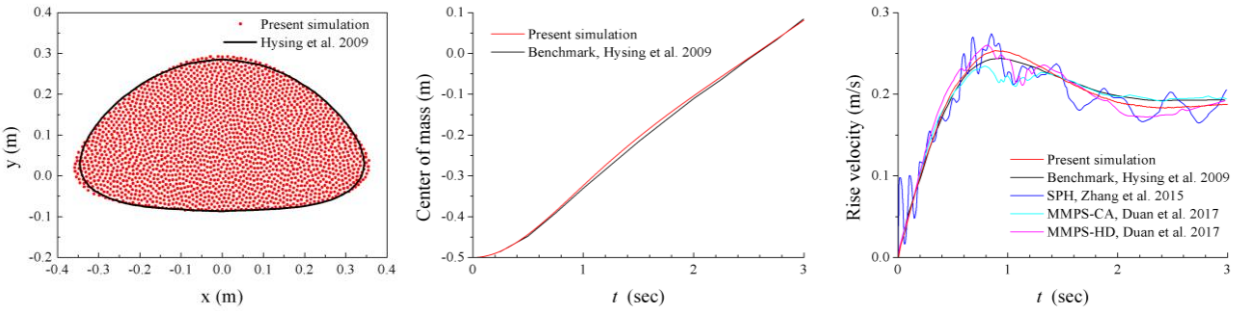

(a) Bubble shape at t = 3 s (b) Center of mass (c) Rising velocity

Figure 12 Comparison of different methods[19]

The bubble shapes simulated by present method at t = 3 s are compared with the benchmarks results in Fig. 12(a), where good agreement is obtained. Furthermore, the results of the evolution of center of mass and rise velocity are presented in Fig. 12(b, c). The bubble rises at a growing speed at the early stage, until a largest velocity appears. After that, the bubble gradually slows down and a steady velocity is finally reached, called terminal velocity. In general, good agreements with benchmark results can be observed.

DNS for Surface-Tension-Driven Interfacial Flows

Direct Numerical Simulation (DNS) demands a high qualification in numerical scheme and mesh scale [20-21]. To maintain the simplicity of Cartesian grid and solving the problem with adequate resolution for interface and microscale turbulence, the low-dissipative method coupled with adaptive mesh refinement (AMR) strategy is naturally advisable [22]. By adopting the AMR strategy, mesh refinement is applied locally according to the flow pattern and the interface location [4-6]. This allows the computational workload to be concentrated only in the crucial region, which greatly improves the computational efficiency. Besides, the uniform grid layout in each block makes it possible to implement high-order schemes without hindrance [23-25], while it is usually complicated under curvilinear or unstructured mesh.

In this study, a two-phase flow solver based on the block-structured adaptive mesh (BAMR) [26-27] with non-overlapped grid topology is developed. The basic unit for manipulation is 'block' as shown Fig. 13(a) (c), in which the computational domain is discretized on a series of block $\mathcal{B}_\mathcal{L}$, $(\mathcal{L} = 0,1, \dots, \mathcal{L}^{max})$. $\mathcal{B}_0$ is the coarsest level and the level $\mathcal{L}+1$ is finer than the level $\mathcal{L}$ with the factor of 2. To manage the block topology efficiently, the octree-based hierarchical data structure is utilized (Fig. 13 (b)). Here we define $\{\mathcal{B}_\mathcal{L} \in \Omega\}$, $\Omega = \Omega_L \cup \Omega_B$, where Ω is the set of all nodes; Ω_L and Ω_B are the set of leaf nodes and branch nodes, respectively. Numerical solution is advanced only on $\{\mathcal{B}_\mathcal{L} \mid \forall \mathcal{B}_\mathcal{L} \in \Omega_L\}$, which is indicated by the solid circles in Fig. 13 (b). Different from the overlapped grid topology, physical memory required by present method is allocated only in $\{\mathcal{B}_\mathcal{L} \mid \forall \mathcal{B}_\mathcal{L} \in \Omega_L\}$, and no memory space is assigned for the nodes marked with dotted circle. The Peano and Hilbert space-filling curves [8] are generated based on the octree for dynamically loading balance among the processors.

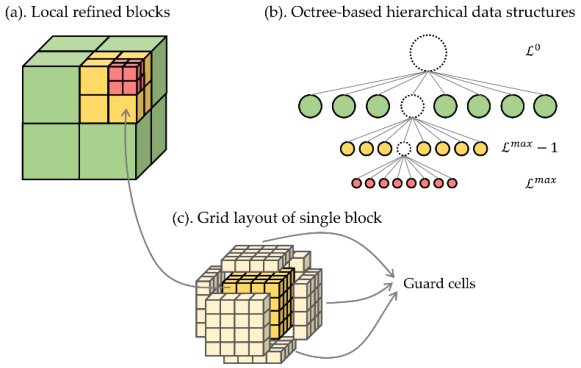

Figure 13 3-D adaptive mesh and its representation as an octree

Solving the pressure Poisson equation is one of the most difficult parts for the two-phase flow AMR solver. Since in this study the graded adaptive mesh is employed, which means the size ratio between adjacent cells is not allowed to be greater than two, discretization of the partial differential operator can be realized by performing 1D interpolation separately in all axial directions. Unlike conventional multigrid (MG) method [28], in which information of the variables defined in the whole hierarchical mesh is required, present Poisson solver uses a fully unstructured

treatment for the adaptively refined Cartesian grids. The overlapped blocks are totally excluded in the formulation of the linear system. By this treatment we are able to use highly efficient mathematical libraries, such as *HYPRE* [29] and *PETSc* [30], etc. Numerical tests show that for a moderate scale linear system (total unknowns less than 10 million) the FGMRES (flexible generalized minimal residual) method with the GAMG (geometric and algebraic multigrid) preconditioner gives the best performance. However, the parallel efficiency of GAMG is limited by the low scalability of the semi-coarsening algorithm. For a large scale parallel computation (total unknowns more than 100 million), the Additive Schwarz method (ASM) based on multi-block matrices shows much more efficient and is recommended.

Main features of our solver are summarized as follows. First, we extend the interface capturing method including THINC[31] and VOF[32]schemes for sharp representation of moving distorted interfaces in adaptive mesh. A prolongation approach by using CIP method is proposed to preserve the flux conservation in newly created cells. Our conservative prolongation treatment is motivated by Chen et al. [33], in which the surface integrated average (SIA) and VIA are utilized to complete the prolongation with the assistant of multi-dimensional Lagrange polynomial interpolation (LPI). The low dissipative multi-moment FVM with a dimensional splitting method is adopted for spatial discretization of governing equations for two-phase flow.

Liquid jet atomization is an important physical process in many industrial applications, for instance, the fuel spray nozzle of automotive engines, chemical rocket propulsion systems and inkjet printing machine etc. In this section, we extend the two-phase flow solver to adapt to large scale parallel computation of high-speed liquid fuel injection. For comparison, the jet atomization problems which has been investigated by J. Shinjo and A. Umemura [34] are recalculated using the new developed BAMR method.

Numerical setup of the fluid properties are taken form reference [34], as given in Table. 1. The injection nozzle is round and flat with the diameter $0.1mm$. Followed with Shinjo and A. Umemura [34], to exclude the effect of inlet turbulence, the injection velocity profiles are assumed to be flat. For Case-I, six levels (level 3~8) adaptive mesh are used, while seven levels (level 3~9) for Case-II. Fig. 14(a) and (b) shows the iso-surface ($C = 0.5$) of volumetric fraction field. Apparently, the higher speed jet (Case-II) creates better atomization effect than the lower speed (Case-I). For numerical simulation, the liquid structures break into parts only when the grid resolution cannot resolve the thickness of the liquid film, which means the numerical atomization is artificially induced. Consequently, a fine mesh is always necessary to bridge the gap between the real and the simulated jet spray. In present study, we use very fine mesh (0.73~1μm) to capture the liquid tip.

Present example is a typical case to demonstrate the high computational efficiency of the BAMR method. Compared with traditional uniform Cartesian gird method [34], the BAMR solver uses a larger computational domain with finer localized refinement to resolve the free surface. Take Case-II as an example, the total grid number for BAMR is only 1/200~1/6 of that for uniform grid [34], while the minimal grid resolution of BAMR are roughly the same (Case-II) even better (Case-I) than uniform mesh [34]. All blocks used for simulation of Case-I and II are filled by 8×8×8 uniform grids of different levels. The HPC cluster in our lab with 80 physical cores (Intel Xeon E5-4627, 3.4GHz) are in use for present parallel computation. A high performance message passing library (*Open MPI*) is applied for data communication among processors. The derived linear system is solved by third-party mathematical libraries *Hypre* [29] and *PETSc* [30].

Table 1. Flow properties for jet spray simulation

Descriptions	We	Re	U (m/s)	D (mm)	Ambient p (MPa)	ρ_g (Kg/m^3)	ρ_l (Kg/m^3)	μ_g (Pa·s)	μ_l (Pa·s)	σ (N/m)
Case-I	1270	440	30	0.1	3	34.5	848	2.87E^{-6}	1.97E^{-5}	3.0E^{-2}
Case-II	3530	740	50							

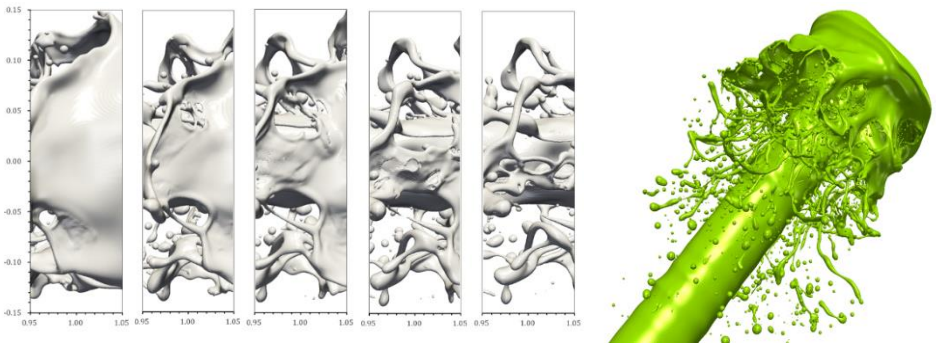

Fig. 14 (a) Breaking-up of the liquid film of for Case-I, (b) instantaneous free surface of liquid jet spray simulations for Case-II.

CONCLUSIONS

In present paper, the CFD simulations of multiphase flow at different scales, including the simulation of cavitation and ship wave breaking (macroscale), bubble flows (mesoscale), single rising-bubble and jet spray (microscale), are demonstrated in detail. The numerical results obtained by those methods are in accordance with the experimental results and other researchers' numerical works. It is concluded that with the in-depth research and development of numerical methods, the present numerical approaches and developed CFD solvers can deal well with complex multiphase flow problems.

In the future, the computational efficiency and accuracy of present methods will be improved to extend it for the high-fidelity prediction of complicated multiphase flows in multiscale.

REFERENCES

[1] Berberović, E., van Hinsberg, N., Jakirlić, S., Roisman, I., and Tropea, C. Drop impact onto a liquid layer of finite thickness: Dynamics of the cavity evolution [J]. Phys. Rev. E, 2009, 79(3), 36306.

[2] Shen, Z., Wan, D.C., and Carrica, P. M. Dynamic overset grids in OpenFOAM with application to KCS self-propulsion and maneuvering [J]. Ocean Eng., 2015, 108, 287–306.

[3] Wang, J., Zou, L., and Wan, D.C. CFD simulations of free running ship under course keeping control[J]. Ocean Eng., 2017, 141, 450–464.

[4] Wang, J., Zhao, W., and Wan, D.C. Development of naoe-FOAM-SJTU solver based on OpenFOAM for marine hydrodynamics [J], J. Hydrodyn., 2019, 31(1), 1–20.

[5] Wang, J., and Wan, D.C. Breaking Wave Simulations of High-speed Surface Combatant using OpenFOAM [C]. Proceedings of the 8th International Conference on Computational Methods, 25-29 Jul. 2017, Guilin, China.

[6] Olivieri, A., Pistani, F., Avanzini, A., Stern, F., Penna, R. Towing tank experiments of resistance, sinkage and trim, boundary layer, wake, and free surface flow around a naval combatant INSEAN 2340 model [R], IIHR Report No. 421, 2019.

[7] Wang, J., Ren, Z., and Wan, D.C. RANS and DDES Computations of High Speed KRISO Container Ship [C]. Proceedings of the 32nd Symposium on Naval Hydrodynamics, 5-10 Aug. 2018, Hamburg, Germany.

[8] Schnerr. G. H, Sauer. J. Physical and numerical modeling of unsteady cavitation dynamics [C], Proceedings of 4th International Conference on Multiphase Flow. New Orleans, USA, 2001.

[9] Reboud, J. L, Stutz. B and Coutier-Delgosha. O. Two Phase FlowStructure of Cavitation Experiment and Modeling of Unsteady Effects [C], Proceedings of 3rd Symposium on Cavitation, Grenoble, France, 1998.

[10] Sundaresan S, Ozel A, Kolehmainen J. Toward Constitutive Models for Momentum, Species, and Energy Transport in Gas–Particle Flows [J]. Annu. Rev. Chem. Biomol. Eng., 2018, 9(1), 060817-084025.

[11] Marchisio, D. L., Fox, R. O. Computational models for polydisperse particulate and multiphase systems [M]. Cambridge University Press, 2013.

[12] Yang N, Wang W, Ge W, et al. CFD simulation of concurrent-up gas–solid flow in circulating fluidized beds with structure-dependent drag coefficient [J]. Chem. Eng. J., 2003, 96(1-3), 71-80.

[13] Yan Y, Jinling L, Kun, Z, Rui W, Shijie Q. Experimental Study of Turbulent Drag Reduction on a Plate Using Microbubbles [J]. Phys.Gases, 2017, 2(4), 29-35.

[14] Wen, X. and Wan, D. C. Numerical simulation of Rayleigh-Taylor instability by multiphase MPS method [J], Int. J. Comp. Meth., 2018, 15(3), 1846005.

[15] Wen, X. and Wan, D. C. Numerical simulation of three-layer-liquid sloshing by multiphase MPS method [C], the ASME 2018 37th International Conference on Ocean, Offshore and Arctic Engineering, OMAE2018, Madrid, Spain, 2018, 78387.

[16] Shakibaeinia, A. and Jin, Y. MPS mesh-free particle method for multiphase flows [J], Comput. Methods Appl. Mech. Engrg., 2012, 229–232, 13–26.

[17] Duan, G., Chen, B., Koshizuka, S. and Xiang, H. Stable multiphase moving particle semi-implicit method for incompressible interfacial flow [J], Comput. Methods Appl. Mech. Engrg., 2017, 318, 636–666.

[18] Hysing, S., Turek, S., Kuzmin, D., Parolini, N., Burman, E., Ganesan, S. and TobiskaL, T. Quantitative benchmark computations of two-dimensional bubble dynamics [J], Int. J. Numer. Meth. Fluids, 2009, 60(11), 1259-1288.

[19] Zhang, A., Sun, P. and Ming, F. An SPH modeling of bubble rising and coalescing in three dimensions [J], Comput. Methods Appl. Mech. Engrg., 2015, 294, 189–209.

[20] Ling Y, Fuster D, Zaleski S, et al. Spray formation in a quasiplanar gas-liquid mixing layer at moderate density ratios: A numerical closeup[J]. Phys. Rev. Fluids, 2017, 2(1), 014005.

[21] Zuzio D, Estivalezes J, Dipierro B, et al. An improved multiscale Eulerian–Lagrangian method for simulation of atomization process[J]. Comput. Fluids, 2016, 285-301.

[22] Popinet S. An accurate adaptive solver for surface-tension-driven interfacial flows[J]. J. Comput. Phys., 2009, 228(16), 5838-5866.

[23] Liu C, Hu C. An adaptive multi-moment FVM approach for incompressible flows[J]. J. Comput. Phys., 2018, 359, 239-262.

[24] Liu C, Hu C. Block-based adaptive mesh refinement for fluid–structure interactions in incompressible flows[J]. Comput. Phys. Commun., 2018, 232, 104-123.

[25] Liu C, Hu C. Adaptive THINC-GFM for compressible multi-medium flows[J]. J. Comput. Phys., 2017, 342, 43-65.

[26] Berger M J, Colella P. Local adaptive mesh refinement for shock hydrodynamics[J]. J. Comput. Phys., 1989, 82(1), 64-84.

[27] Macneice P J, Olson K M, Mobarry C, et al. PARAMESH: A parallel adaptive mesh refinement community toolkit[J]. Comput. Phys. Commun., 2000, 126(3), 330-354.
[28] Trottenberg U, Oosterlee C W, Schuller A. Multigrid. Academic Press, 2000.
[29] Falgout R D, Yang U M. hypre: A library of high performance preconditioners [C]. International Conference on Computational Science. Springer Berlin Heidelberg, 2002, 632-641.
[30] Balay S, Brown J, Buschelman K, et al. PETSc users manual revision 3.4 [R]. Computer Science Division, Argonne National Laboratory, Argonne, IL, 2012.
[31] Xiao F, Honma Y, Kono T, et al. A simple algebraic interface capturing scheme using hyperbolic tangent function[J]. Int. J. Num. Meth. Fluids, 2005, 48(9), 1023-1040.
[32] Kawano A. A simple volume-of-fluid reconstruction method for three-dimensional two-phase flows[J]. Comput. Fluids, 2016, 130-145.
[33] Chen C, Xiao F, Li X, et al. An Adaptive Multimoment Global Model on a Cubed Sphere[J]. Mon. Weather Rev., 2011, 139(2), 523-548.
[34] Shinjo J, Umemura A. Surface instability and primary atomization characteristics of straight liquid jet sprays [J]. Int. J. Multiphase Flow, 2011, 37(10), 1294-1304.